

A Bidirectional Series Resonant Matrix Converter Topology for Electric Vehicle DC Fast Charging

José Juan Sandoval
Student Member, IEEE

Somasundaram Essakiappan
Member, IEEE

Prasad Enjeti
Fellow, IEEE

Department of Electrical & Computer Engineering, Texas A&M University, College Station, USA
e-mail: enjeti@tamu.edu

Abstract—A series resonant matrix converter (MC) based topology for high power electric vehicle (EV) battery charging is presented. The system performs DC fast charging and is capable of bidirectional power flow, for $V2G$ (vehicle-to-grid) applications. The proposed topology can be divided into three sections: (i) a front-end 3x1 matrix converter, (ii) L_rC_r series resonant tank and high frequency (HF) transformer, and (iii) a single phase PWM rectifier. The matrix converter takes a three phase line frequency voltage and produces a high frequency (14.94 kHz) AC output. The resonant tank frequency is set to 13.7 kHz and helps to achieve zero voltage switching (ZVS) turn ON and low turn OFF switching losses. The secondary of the transformer is then interfaced to the EV battery bank through a PWM rectifier. The advantages of such a system include high efficiency due to soft switching operation, low VA transformer ratings due to resonant operation, and high power density due to the absence of electrolytic capacitors. A design example rated 30 kW, which charges a 500 V battery system, is presented. Analysis and simulation results demonstrate the performance of the proposed bidirectional topology. Preliminary experimental results are provided for a scaled down prototype operating at 500 W using a 15 kHz ferrite transformer.

Keywords—matrix converter, zero voltage switching, series resonant tank, electric vehicle, DC fast charging, $V2G$

I. INTRODUCTION

THE motivation to become more independent of fossil fuels, and provide cleaner personal transportation alternatives has led to increased production of plug-in electric (PEV) and electric vehicles (EV). With initiatives such as the *EV Everywhere Grand Challenge*, it is expected that PEVs and EVs will play a significant role in the personal transportation sector [1]. To achieve greater market penetration of these technologies, improvements have to be made in batteries, electric drivetrain systems and charging infrastructure. It is well known that the acceptance of EVs by consumers is deeply affected by charging times [2, 3]. The ability to fully charge the batteries in long-range EVs, within a reasonably short period of time is crucial to accelerate mass adoption. This opens up a wide window of research opportunities in battery fast-charging power electronic topologies. Such topologies must be highly efficient, highly reliable, and cost-effective, in addition to having very high input power quality.

$V2G$ (Vehicle-to-Grid), or bidirectional power flow capability, is another facet of the burgeoning EV charging infrastructure. The motivations for $V2G$ and its benefits have been comprehensively identified before, [4, 5] including:

improved and reliable utility supply, better load following, revenue potential for the vehicle owner, and renewables capacity firming. Employing DC fast charging topologies for $V2G$ applications has been increasingly of interest to researchers. As of date of this publication, technology validation of $V2G$ using DC fast chargers has been performed [6, 7]. In addition, pilot programs using multiple $V2G$ – DC fast chargers are in progress [8]. As $V2G$ – DC fast chargers become mainstream, the development of high-efficiency, highly compact bidirectional systems becomes crucial.

DC fast charging topologies have been previously proposed in [9, 10] which use simple topologies or easy-to-use control systems. Various high power density solutions which achieve high power factor operation are presented in [11]. However, they often use electrolytic capacitors on the DC link potentially decreasing the reliability of the system [12], and they lack bidirectional power flow capability. In [13], an MC based topology is proposed, which eliminates the need for an electrolytic capacitor while achieving power quality and bidirectional power flow. Nonetheless, this topology uses 12 semiconductor devices operated in hard switching mode, which leads to a decrease in the system efficiency due to switching losses.

The proposed MC based battery charging topology seeks to overcome the limitations of existing solutions by employing soft switching techniques and being able to perform $V2G$ power transfer. The proposed architecture has many advantages:

- Bidirectional high power flow between utility grid and battery bank for $V2G$.
- Soft switching of MC semiconductor switches greatly reduces turn ON and turn OFF losses, increasing system efficiency, even though the topology still uses 12 semiconductor devices in the front-end converter.
- The use of an L_rC_r resonant tank leaves the transformer to process only selected frequencies, thereby decreasing its VA rating requirement.
- Direct AC/AC conversion via MC eliminates the need for electrolytic capacitors and potentially increases reliability and power density of the system.
- The use of high frequency (HF) transformer also increases power density, while providing galvanic isolation.

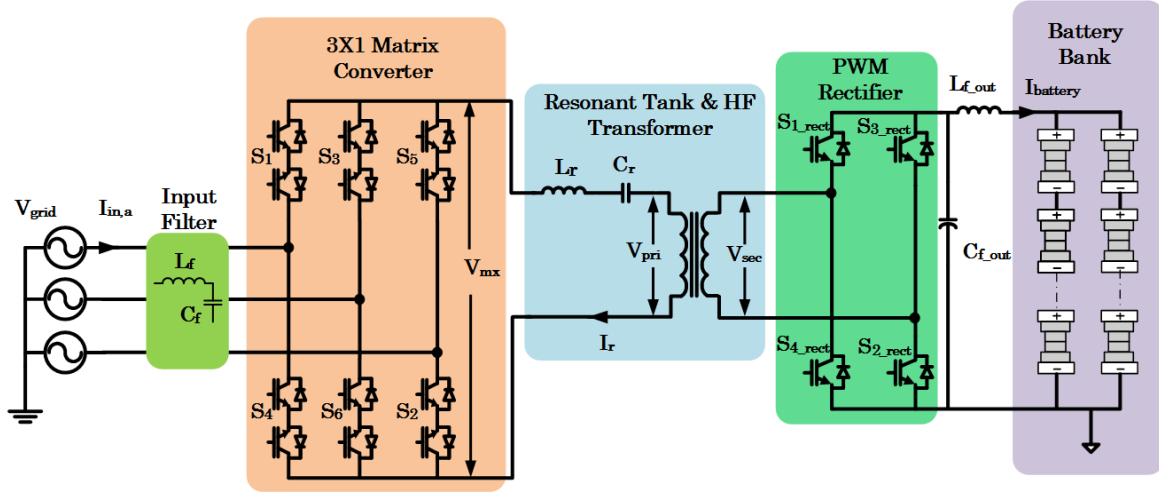


Fig. 1. Proposed series resonant MC topology for EV battery charging. MC semiconductor switches are turned ON at zero voltage and turned OFF at low currents. This topology is capable of bidirectional power flow between the grid and battery bank.

II. PROPOSED MATRIX CONVERTER TOPOLOGY FOR DC FAST CHARGING

The proposed topology for EV battery charging uses a high frequency transformer for power processing as shown in Fig.1. The topology can be divided into three stages: (A) 3x1 matrix converter, (B) $L_r C_r$ resonant tank and HF transformer, and (C) a single phase PWM rectifier.

A. 3x1 Matrix Converter

The three phase utility grid is interfaced to the MC via an $L_f C_f$ filter. The MC consists of six bidirectional switches (S_1 - S_6) as shown in Fig.1. The converter takes a line frequency three phase sinusoidal input voltage and delivers a high frequency quasi-square wave output. S_1 - S_6 are capable of operating in all four quadrants of the V-I plane by virtue of their construction.

Different modulation techniques for the 3x1 MC have been studied in [13-16]. The modulation technique proposed for this topology has been described in [13]. A unipolar SPWM switching function, S_{AB} , is obtained from two bipolar SPWM signals, PWM_A and PWM_B ($S_{AB} = PWM_A - PWM_B$). The resulting S_{AB} , seen in (1), is then multiplied by a square wave switching function S_{inv} , seen in (2), to produce the resultant switching function of the MC, as illustrated in Fig. 2. This resultant switching function F_1 of the bidirectional switch S_1 is

the product of unipolar SPWM and a square wave with high frequency f_{sq} , as seen in (3).

Unipolar switching functions S_{BC} and S_{CA} are shifted 120° and 240° (of the line frequency) respectively compared to S_{AB} . Switching functions F_2 and F_3 are the products of S_{BC} and S_{CA} with S_{inv} respectively (seen in (4) and (5)). From switching functions F_1 - F_3 , the gating signals for the devices S_1 - S_6 are obtained. When F_1 is positive S_1 is turned ON, and when F_1 is negative S_4 is turned ON. Similarly F_2 and F_3 determine the gating signals for the devices in the second and third half-bridges in the matrix converter respectively. There are instances where F_1 , F_2 and F_3 are all zero simultaneously. During these zero states one of the three half-bridges is shorted to provide a freewheeling path for the transformer current. Hence the output of the MC is described by (6).

$$V_{mx} = F_1 \cdot V_{an} + F_2 \cdot V_{bn} + F_3 \cdot V_{cn} \quad (6)$$

where V_{an} , V_{bn} and V_{cn} are the utility line-to-neutral voltages. The output of the MC has a quasi-square wave nature. The fundamental component of the voltage produced by the MC is given by (7)

$$V_{mx,1} = \frac{3}{2} \sqrt{\frac{2}{3}} 0.866 \cdot \frac{4}{\pi} m_a \cdot V_{LL} \quad (7)$$

$$S_{AB} = m_a \cdot \left[0.866 \sin(2\pi f_{grid} t) + 0.275 \sin(2\pi \{m_f \pm 2\} f_{grid} t) + 0.01548 \sin(2\pi \{m_f \pm 4\} f_{grid} t) \right. \\ \left. + 0.157 \sin(2\pi \{2m_f \pm 1\} f_{grid} t) + \dots \right] \quad (1)$$

$$S_{inv} = \sum_{n=1,3,5,\dots}^{\infty} \frac{4}{\pi} V_{sq} \sin(2n\pi f_{sq} t) \quad (2)$$

$$F_1 = S_{AB} \cdot S_{inv} \quad (3)$$

$$F_2 = S_{BC} \cdot S_{inv} \quad (4)$$

$$F_3 = S_{CA} \cdot S_{inv} \quad (5)$$

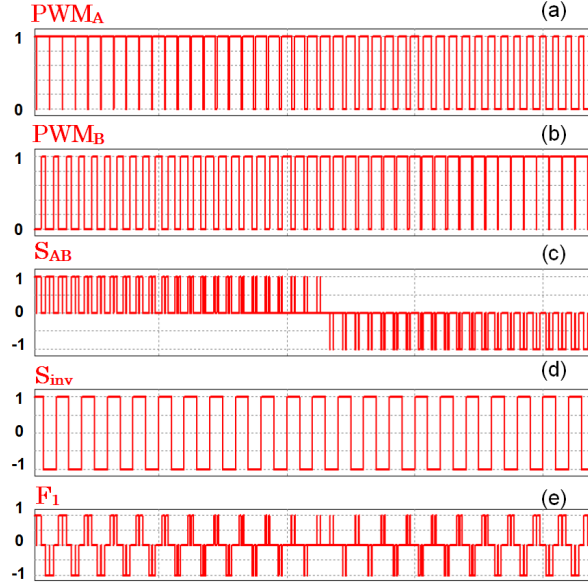


Fig. 2. (a) PWM_A obtained by comparing a high frequency (14.94 kHz) carrier wave with a line frequency sinusoidal modulating function. (b) PWM_B obtained as in (a) but modulating function has a 120° phase shift. (c) Switching function S_{AB} is the subtraction $PWM_A - PWM_B$. (d) S_{inv} is a high frequency square wave switching function. This frequency determines the output frequency of the MC (e) Overall switching function is the product of S_{AB} and S_{inv} .

B. Resonant Tank and High Frequency Transformer

An $L_r C_r$ resonant tank is connected across the output of the MC in series with the HF transformer primary. The resonant tank frequency is set to 13.7 kHz and helps to achieve ZVS turn ON conditions and low turn OFF switching losses. The resonant capacitor C_r also serves to block any DC voltage preventing core saturation. The square wave frequency, f_{sq} , used for modulation of the MC is set above the resonant frequency of the $L_r C_r$ tank which is given by (8).

$$f_r = \frac{1}{2\pi\sqrt{L_r C_r}} \quad (8)$$

Since the output of the MC is a quasi-square wave with frequency close to resonance, the current through the filter tank, I_r , has a sinusoidal nature with frequency f_{sq} . The magnetizing inductance of the transformer does not play a role in the resonance of the tank but it has an effect on the voltage across the primary. The fundamental component of the voltage across the primary is given by (9).

$$V_{pri,1} = \frac{X_{Lm} \cdot R_{eq} \cdot V_{mx,1}}{\sqrt{(R_{eq} [X_{Lr} + X_{Lm} - X_{Cr}])^2 + (X_{Lm} (X_{Lr} - X_{Cr}))^2}} \quad (9)$$

where R_{eq} is effective impedance referred to the primary side. X_{Lm} , X_{Cr} , X_{Lr} are the reactances of the magnetizing inductance, resonant tank capacitor, and resonant tank inductor respectively.

The dependency of voltage gain of the series resonant tank on operational frequency is shown in Fig. 3. The normalized frequency f_n is the ratio of the operating square wave frequency f_{sq} to the resonant frequency f_r . As anticipated, the voltage gain is unity at resonant frequency, since the resonant tank impedance is at a minimum at this frequency and the resistance component is dominant. It can also be observed that operating above resonance, the voltage gain is less than unity.

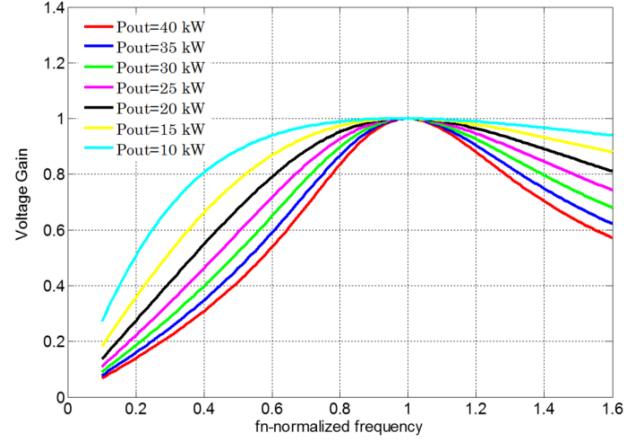


Fig. 3. Voltage gain-frequency curves of series resonant tank. Operating above resonance yields a gain < 1 . Furthermore, operating above the resonant frequency enables ZVS turn ON and low turn losses.

An HF transformer was designed for a 500 W scaled-down prototype. Due to its low cost and moderate power loss [17], a ferrite magnetic core material is selected. To avoid saturation, the operational magnetic flux density of the selected core is limited to 0.25 T and the magnetic flux intensity to 60 Am^{-1} . At this operating point, the magnetic permeability of the core is 0.004 Hm^{-1} . The characteristics of the ferrite core chosen for this application are given in Table 1.

TABLE 1: FERRITE CORE CHARACTERISTICS

Core type	3C85
Maximum flux density, B_{max}	0.4 T at 25 °C
Effective cross sectional area, A_e	0.000625 m^2
Effective magnetic path length, l_e	0.42 m
Power loss, P_v	150 W m^{-3} at 15 kHz
Density	4800 kg m^{-3}

In order to determine the number of turns in the primary side (N_{pri}), the relationship shown in (10) is used.

$$V_{pri} = 4 \cdot B \cdot A_e \cdot N_{prim} \cdot f \quad (10)$$

The number of turns in the primary is set to 30 which achieves 281V on the primary side. The expected magnetizing inductance is determined by (11).

$$L_m = \frac{\mu \cdot N^2 A_e}{l_e} \quad (11)$$

The magnetizing inductance of the designed transformer was calculated to be 6.7 mH. The worst case magnetizing current (i_m) for an applied voltage of 300 V is 0.5 A. The magnetic field intensity is found by (12). The value at this operating point is calculated to be 32 A m^{-1} which is below the 60 A m^{-1} saturation limit.

$$H = \frac{N \cdot i_m}{l_e} \quad (12)$$

The transformer turns ratio is a factor of the required output voltage. The prototype is designed for a 450 V output. Since the primary side can reach 281 V, the turns ratio ($n_1:n_2$) must be at least 1:1.6. In order to account for conduction losses, the transformer turns ratio is set to 1:1.7. Performing a transformer short circuit test, the leakage inductance $L_{leakage}$ was measured to be 4 μ H. Similarly, an open circuit test yielded a magnetizing inductance L_m of 4.6 mH. The resonant tank and transformer frequency characteristics are experimentally obtained using a frequency response analyzer and the results are produced. The Bode gain and phase plots are shown in Fig. 4 and the impedance characteristics are in Fig. 5. It can be verified that the gain reaches unity at the resonant frequency. Likewise, the resonant tank and transformer impedance is at its minimum when the frequency reaches resonance. The inductance used for the resonant tank L_r is 23 μ H and the capacitance C_r is 4.3 μ F.

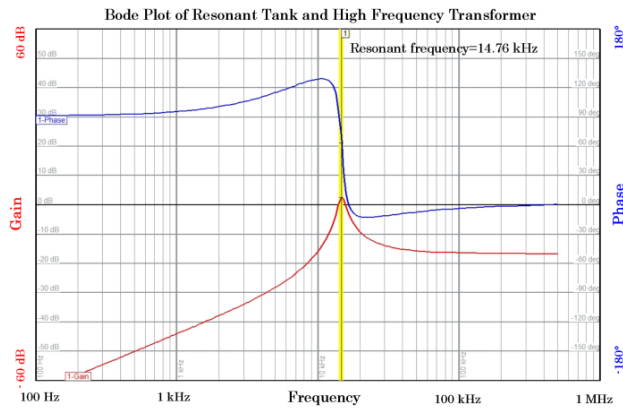


Fig. 4. Frequency response of resonant tank and high frequency transformer showing a notch-filter type performance. The gain reaches unity (0 dB) at the resonant frequency as expected and other frequencies are attenuated. The phase approaches zero as the frequency gets close to resonance. ($L_r=23 \mu$ H, $C_r=4.3 \mu$ F, $L_{leakage}=4 \mu$ H, $L_m=4.6$ mH).

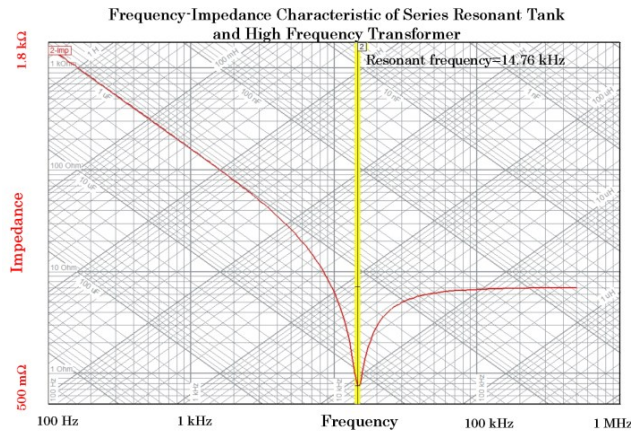


Fig. 5. Impedance characteristic of resonant tank and high frequency transformer. As expected, the impedance reaches its minimum value at the resonant frequency.

C. Single Phase PWM Rectifier

The $L_r C_r$ resonant tank is interfaced to a single phase PWM rectifier via the HF transformer. The single phase PWM rectifier is operated in close loop to regulate the battery current, $I_{battery}$. The rectifier is operated with square wave PWM at the same frequency as f_{sq} . The power transfer is determined by the phase angle difference between the secondary winding voltage and the voltage imposed by the rectifier, akin to a dual active bridge operation. The current flowing through the secondary of the transformer is a high frequency sinusoid; for grid to vehicle ($G2V$) operation when the current is positive the antiparallel diodes of S_{1_rect} and S_{2_rect} conduct, when the current is negative the antiparallel diodes of S_{3_rect} and S_{4_rect} conduct. For $V2G$ operation, the corresponding IGBTs perform current conduction.

III. DESIGN EXAMPLE AND SIMULATION RESULTS

A 30 kW fast-charging design example for a 500 V battery is considered, to demonstrate the operation of the proposed bidirectional series resonant MC in Fig. 1. The parameters in Table II were used for analysis and simulation.

TABLE II: SPECIFICATIONS & OPERATING CONDITIONS USED FOR SERIES RESONANT MC DESIGN EXAMPLE

Grid voltage (line-to-line rms)	480 V
Battery open circuit voltage (OCV)	500 V _{dc}
Rated power	30 kW
Square wave switching frequency (f_{sq})	14.94 kHz
Resonant tank frequency (f_r)	13.7 kHz
Resonant Inductor (L_r)	240 μ H
Resonant Capacitor (C_r)	0.56 μ F

Simulations of the proposed topology in Fig. 1 are performed for two modes of operation: (A) $G2V$ (Grid-to-vehicle mode, charging), in which power flows from the utility grid to the vehicle's battery bank, (B) $V2G$ (Vehicle-to-grid mode, discharging), in which power flows from the battery bank to the utility grid. $G2V$ mode is operated at a maximum power of 30 kW and $V2G$ mode processes a maximum of 15 kW. The analysis is performed both in steady state and in transient between the two operating modes.

A. $G2V$ Mode of Operation

In this mode of operation, the utility grid supplies power to the EV battery bank. The battery voltage and battery current in simulation are shown in Fig. 6. It can be observed that the battery current has very low ripple, with an AC rms value less than 1 A. Fig. 7(a) shows the line-to-neutral voltages and Fig. 7(b) shows the input line currents; the line-to-neutral voltages and the line currents are in phase achieving high displacement power factor. In addition, the THD of the input currents is less than 3%, which makes the system power factor very close to unity.

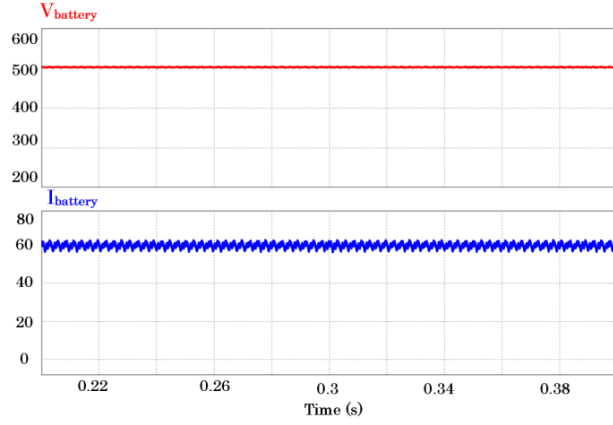


Fig. 6. Battery current (60 A) and voltage (500 V) shown in charging ($G2I$) mode. The output power is 30 kW. The battery current has negligible ripple with an AC rms < 1 A.

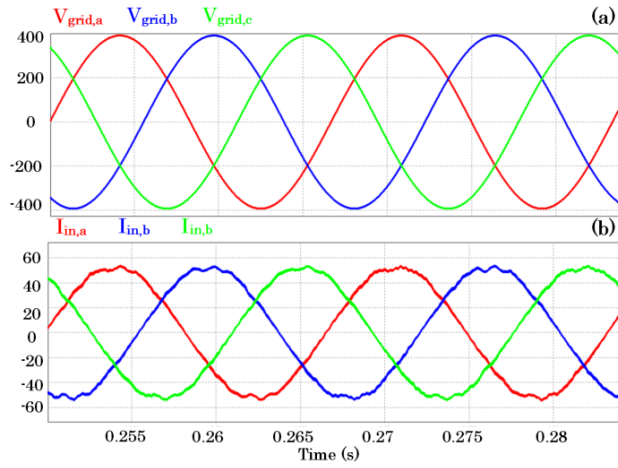


Fig. 7. (a) Line-to-neutral input voltages. (b) Line input currents (rms 36 A). It can be observed that the line currents are in phase with the line-to-neutral voltages. Simulated power factor is 0.99 and simulated THD of the currents is less than 3%.

The output voltage of the 3x1 MC and the resonant tank current, I_r , are shown in Fig. 8(a). The quasi-square wave nature of the voltage can be appreciated. It can also be observed that the current lags the voltage, as one would expect from the inductive nature of the tank at above-resonance operation. The sinusoidal nature of the current I_r can be observed. The frequency spectrum of the matrix converter voltage and the resonant tank current, seen in Fig. 8(b), show the fundamental component at 14.94 kHz as expected. Furthermore, the HF transformer only processes the selected frequency (14.94 kHz) which contributes to a reduction of its VA rating.

Soft switching operation of the topology can be appreciated from Fig. 9, which shows the current through one of the four-quadrant switching devices and the voltage across that device. From the figures, it is evident that the antiparallel diode of a switch conducts before the switch. This means that the switch is turning ON at zero voltage. Similarly, the device turns OFF at zero voltage. Similar ZVS operation may be observed in all other switching devices.

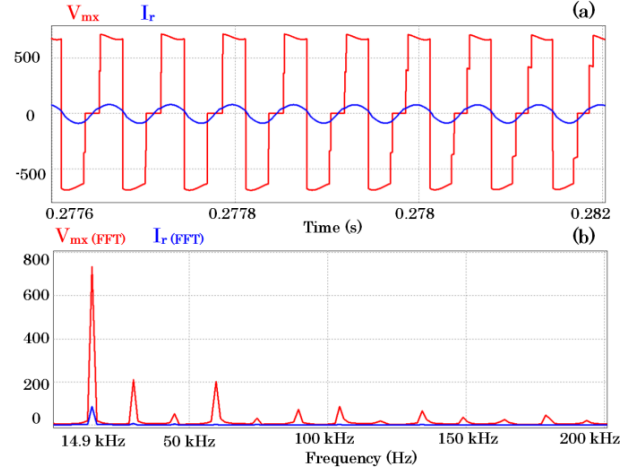


Fig. 8. (a) Output voltage of matrix converter and resonant tank current. The square wave nature of V_{mx} can be observed. (b) The FFT of V_{mx} and I_r show the high frequency operation of the transformer. The transformer responds only to the resonant frequency. The $L_r C_r$ tank blocks all other components since it presents higher impedance to all other frequencies.

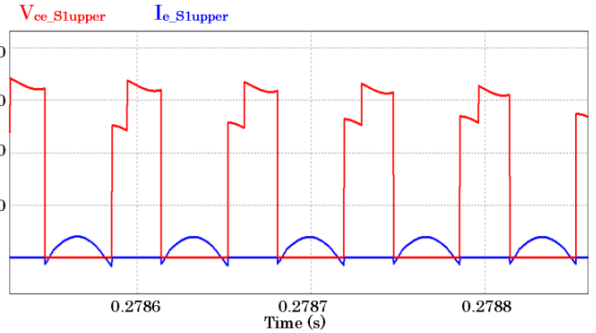


Fig. 9. Soft switching operation of the semiconductor S_{1_upper} . The device turns ON and OFF at zero voltage. Other semiconductor devices operate in similar manner. The device V_{CE} voltage reaches the amplitude of the line-line voltage. Note the absence of ringing in V_{CE} due to soft-switching.

A step response of the battery current, $I_{battery}$, is obtained to verify the robustness of the control strategy. The battery current reference is changed from 60 A to 30 A in a rapid manner, which is not expected in real world EV charging system. However this helps to verify the controller performance. The battery voltage and battery current during this transient are shown in Fig. 10. The battery voltage shown here is the terminal voltage of the battery, which includes voltage drops across the battery equivalent resistance, hence it displays a step change when the charging current is changed. It may also be seen that the phase angle between the transformer secondary voltage and the input terminal voltage of the PWM rectifier is changed by the controller in response to the step change in the battery current reference. Fig. 11 shows the line input currents during the step response, decreasing in amplitude in a smooth manner. Fig. 11 also shows the calculated power factor which remains at unity and only displays a very short reduction during the transient.

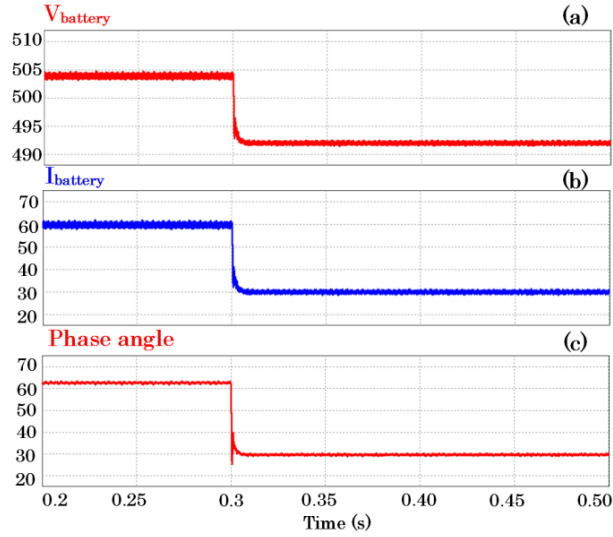


Fig. 10. (a) Battery terminal voltage, (b) battery charging current, and (c) phase angle between secondary voltage and rectifier input terminal voltage. The phase angle is changed in response to the current reference change.

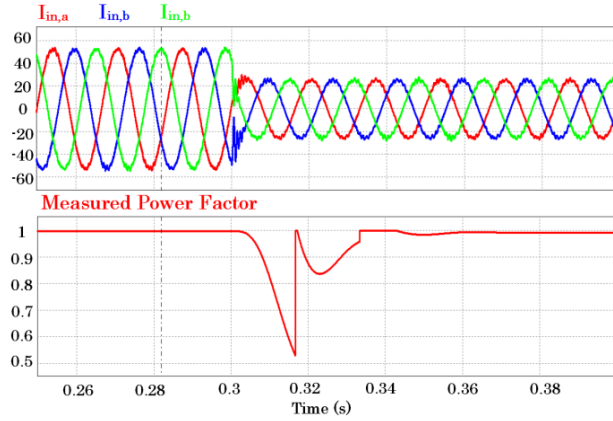


Fig. 11. Three phase line input currents and measured input power factor during transient. The input current quality remains very high (less than 3% THD) and the power factor only displays a short reduction during transient.

B. V2G Mode of Operation

During this mode, the EV battery bank is supplying power to the utility grid. Fig. 12 shows the battery voltage and current during discharging operation, with the battery current being negative, as one would expect. As in the charging mode, the battery current has a very low AC rms value – less than 1 A. Fig. 13 shows the grid line-to-neutral voltages and the input line currents. It can be noted that the currents have a phase shift of 180° with respect to the line-to-neutral voltages, which demonstrates V2G operation. In this mode of operation, the line currents THD is also less than 5%.

In this mode of operation, the semiconductor devices of the MC also operate under soft switching conditions. Fig. 14 (a) shows the V_{CE} voltage across the upper switch S_1 and the current I_e flowing through the device. Similarly, Fig. 14(b) shows the voltage across S_{1_rect} of the PWM rectifier. The figure shows that the device turns ON and OFF under ZVS conditions.

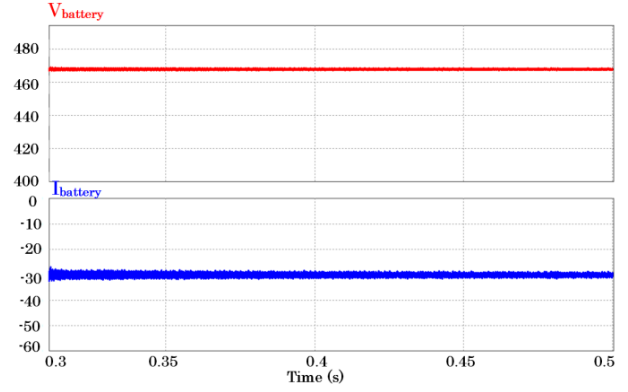


Fig. 12. Battery voltage and battery current during V2G mode. As expected, the battery voltage drops during discharging mode and the current is negative.

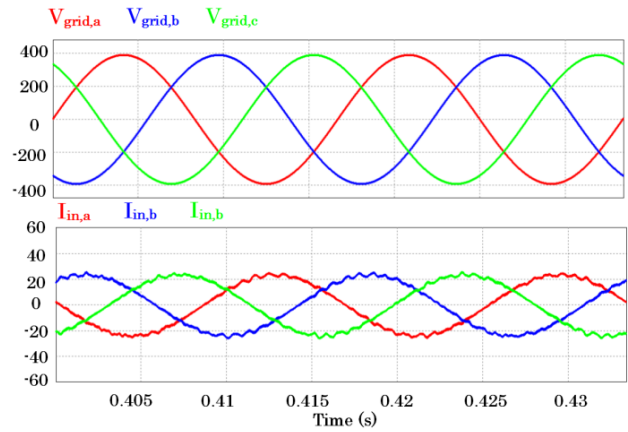


Fig. 13. Line-to-neutral input voltages and line input currents. The currents are 180° phase shifted with respect to the voltages implying power flow to the grid. The line currents waveforms are of high quality, with THD less than 5%.

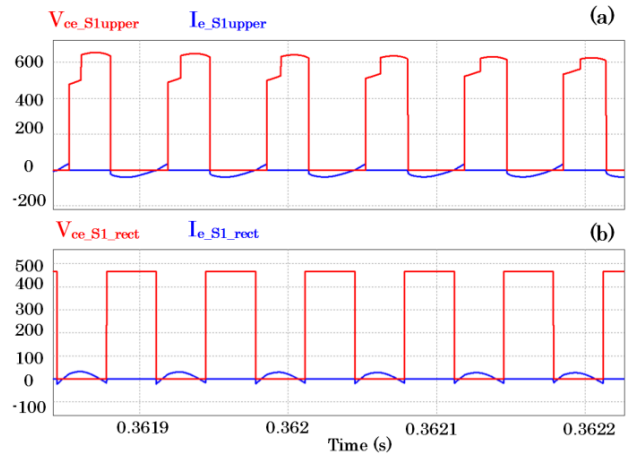


Fig. 14. (a) MC device voltage and current and (b) PWM rectifier device voltage and current. The devices turn ON and OFF at zero voltage. The rest of the devices in the PWM rectifier exhibit similar operational performance.

The step response of the system as it rapidly enters discharging mode from charging mode is shown in Fig. 15. The battery terminals display a predictable voltage drop as it enters discharging mode.

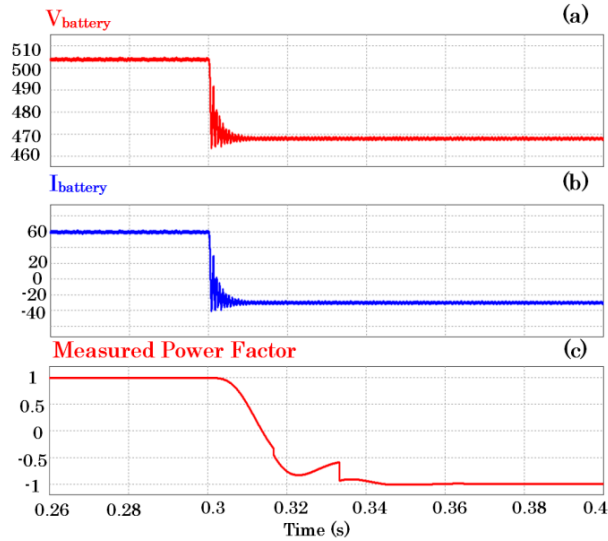


Fig. 15. (a) Battery terminal voltage, (b) battery current, (c) measured power factor, as the system moves from $G2V$ to $V2G$. The measured power factor changes from positive to negative unity during this transient.

The measured power factor of the system, which was unity in $G2V$ mode becomes negative unity in $V2G$ which means the input line currents are out-of-phase with the line-to-neutral voltages.

IV. PRELIMINARY EXPERIMENTAL RESULTS

A scaled-down prototype of the $L_r C_r$ resonant tank and a HF transformer, rated at 500 W, was built and tested in the laboratory. The resonant inductor was designed using an amorphous “Metglas®” core which provides low loss and high saturation flux density. The resonant inductor was designed to be 23 μH , so that along with the HF transformer leakage inductance of 4.15 μH it produces an overall inductance of 27.15 μH . The resonant capacitor value was calculated to be 4.2 μF . The resonant frequency of this set up was 14.9 kHz. The front-end converter for the resonant tank – transformer is a full bridge inverter. The secondary side of the HF transformer was connected to a silicon carbide diode rectifier. The diode rectifier has essentially zero reverse recovery losses. The gate drive signals for the front-end converter were generated using a Texas Instruments TMS320F28335 microcontroller.

Fig. 16 shows the resonant tank current, the voltage across the secondary winding, the voltage (V_{CE}) across one of the semiconductor devices, and the current (I_e) through that device. The sinusoidal nature of the resonant tank current can be appreciated from the figure. Fig. 17 presents a detailed version of Fig. 16 illustrating soft switching operation in the front-end full bridge inverter. It can be observed that the device turns ON under ZVS conditions and encounters a small switching loss during turn OFF. The switching and conduction losses in the semiconductor device can be observed in the multiplication of V_{CE} and I_e waveforms of the device. Fig. 18 shows that at the switching instances the power loss is minimal and conduction losses are as expected. Overall, this device is seen to have a loss of 2.2 W.

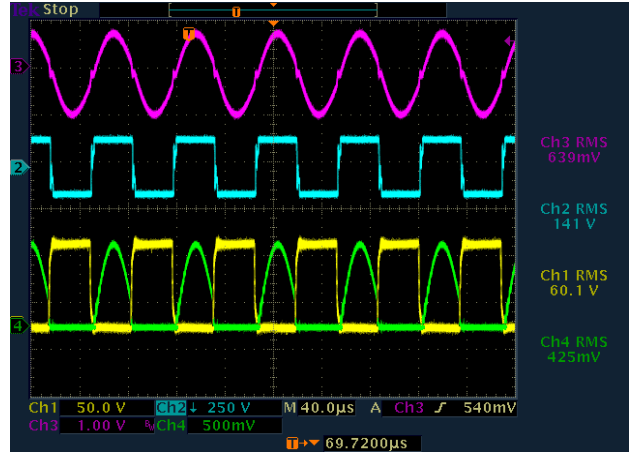


Fig. 16. Resonant tank current I_r (Ch3: 1 div = 10 A), HF transformer secondary voltage (Ch2: 1 div = 250 V), device voltage V_{CE} (Ch1: 1 div = 50 V) and device current I_e (Ch4: 1 div = 5 A).

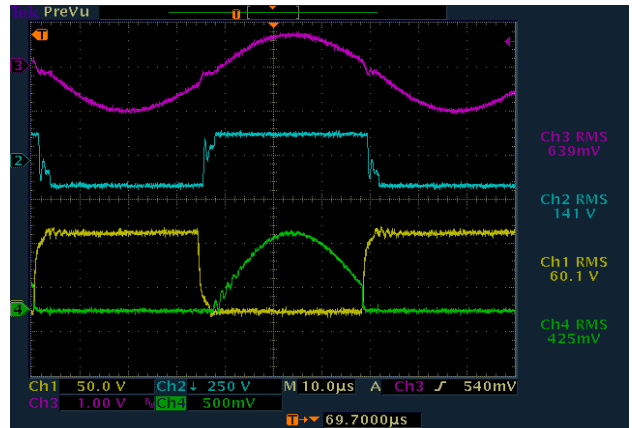


Fig. 17. Detailed version of Fig. 16 to appreciate the soft switching operation. The device current I_e (Ch4: 1 div = 5 A) turns ON at zero voltage and the turn OFF current is low.

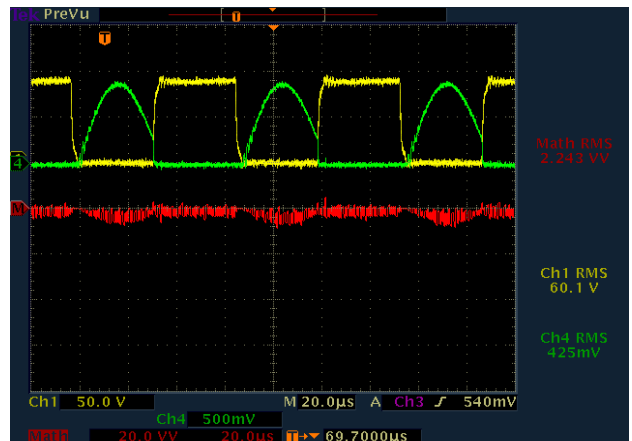


Fig. 18. Multiplication of device voltage V_{CE} (Ch1: 1 div = 50 V) and device current I_e (Ch4: 1 div = 5 A) results in the power loss of the semiconductor device and can be observed in channel M. At switching instances the power loss is near-zero due to soft-switching. Conduction losses occur as anticipated.

V. CONCLUSION

A bidirectional series resonant MC topology for electric vehicle DC fast charging was introduced. The proposed topology has many advantages over existing fast charging architectures such as bidirectional power flow capability, ZVS turn ON and low turn OFF losses which increase efficiency, and high power factor operation. The operation of the proposed topology was described along with extensive analysis of the resonant tank. A design example of a 30 kW/500 V MC EV battery charger was presented and simulation results illustrate the operation of the proposed architecture in both $G2V$ and $V2G$ modes. Preliminary experimental results on a 500 W scaled down high frequency transformer and $L_r C_r$ resonant tank were provided. It was demonstrated that the semiconductor devices operated under soft switching conditions enabling high system efficiency. The front-end 3x1 MC with soft switching capabilities is currently under development.

REFERENCES

- [1] United States Department of Energy, "Vehicle Technologies Office: Plug-in Electric Vehicles and Batteries". Available: <http://energy.gov/eere/vehicles/vehicle-technologies-office-plug-electric-vehicles-and-batteries> [Accessed on: June 2, 2014].
- [2] Wang Shuo, R. Crosier, and Chu Yongbin, "Investigating the power architectures and circuit topologies for megawatt superfast electric vehicle charging stations with enhanced grid support functionality," in *IEEE International Electric Vehicle Conference (IEVC)*, 2012, pp. 1-8.
- [3] A. G. Boulanger, A. C. Chu, S. Maxx, and D. L. Waltz, "Vehicle Electrification: Status and Issues," *Proceedings of the IEEE*, vol. 99, pp. 1116-1138, 2011.
- [4] Briones, A, Francfort, J, Heitmann, P, Schey, M, Schey, S, and Smart, J, (2012) "Vehicle-to-Grid (V2G) Power Flow Regulations and Building Codes Review by the AVTA". Available: http://www1.eere.energy.gov/vehiclesandfuels/avta/pdfs/evse/v2g_power_flow_rpt.pdf [Accessed on: June 7, 2014].
- [5] H. Chaudhry and T. Bohn, "A V2G application using DC fast charging and its impact on the grid," in *IEEE Transportation Electrification Conference and Expo 2012*, pp. 1-6.
- [6] Liu Yaxi and S. C. Mitchem, "Implementation of V2G technology using DC Fast Charging," in *International Conference on Connected Vehicles and Expo*, 2013, pp. 734-735.
- [7] Yutaka Ota, Haruhito Taniguchi, Jumpei Baba, and Akihiko Yokoyama, "Implementation of autonomous distributed V2G to electric vehicle and DC charging system," *Electric Power Systems Research*, 13 June 2014.
- [8] Mark Kane, "Real World Test of V2G Now Underway in Spain". Available: <http://insideevs.com/real-world-test-of-v2g-now-underway-in-spain-wvideo/> [Accessed on: November 14, 2014].
- [9] A. S. Yilmaz, M. Badawi, Y. Sozer, and I. Husain, "A fast battery charger topology for charging of electric vehicles," in *IEEE International Electric Vehicle Conference (IEVC)*, 2012, pp. 1-5.
- [10] Zhang Zuzhi, Xu Haiping, Shi Lei, Li Dongxu, and Han Yuchen, "A unit power factor DC fast charger for electric vehicle charging station," in *7th International Power Electronics and Motion Control Conference (IPEMC)*, 2012, pp. 411-415.
- [11] T. Soeiro, T. Friedli, and J. W. Kolar, "Three-phase high power factor mains interface concepts for Electric Vehicle battery charging systems," in *Twenty-Seventh Annual IEEE Applied Power Electronics Conference and Exposition (APEC)*, 2012, pp. 2603-2610.
- [12] S. Harb and R. S. Balog, "Reliability of Candidate Photovoltaic Module-Integrated-Inverter (PV-MII) Topologies - A Usage Model Approach," *IEEE Transactions on Power Electronics*, vol. 28, pp. 3019-3027, 2013.
- [13] H. S. Krishnamoorthy, P. Garg, and P. N. Enjeti, "A matrix converter-based topology for high power electric vehicle battery charging and V2G application," in *38th Annual Conference on IEEE Industrial Electronics Society*, 2012, pp. 2866-2871.
- [14] S. Manias and P. D. Ziogas, "A Novel Sinewave in AC to DC Converter with High-Frequency Transformer Isolation," *IEEE Transactions on Industrial Electronics*, vol. IE-32, pp. 430-438, 1985.
- [15] S. Ratanapanachote, Cha Han Ju, and P. N. Enjeti, "A digitally controlled switch mode power supply based on matrix converter," *IEEE Transactions on Power Electronics*, vol. 21, pp. 124-130, 2006.
- [16] V. Vlatkovic, D. Borojevic, and F. C. Lee, "A zero-voltage switched, three-phase isolated PWM buck rectifier," *IEEE Transactions on Power Electronics*, vol. 10, pp. 148-157, 1995.
- [17] She Xu, A. Q. Huang, and R. Burgos, "Review of Solid-State Transformer Technologies and Their Application in Power Distribution Systems," *IEEE Journal of Emerging and Selected Topics in Power Electronics*, vol. 1, pp. 186-198, 2013.